




Sputtered Ag-doped NiO thin films: structural, optical, and electrocatalytic activity toward methanol oxidation

Mohamed Sh. Abdel-wahab^{1,*} , Hadeer K. El Emam¹, and Waleed M. A. El Rouby¹

¹Materials Science and Nanotechnology Department, Faculty of Postgraduate Studies for Advanced Sciences, Beni-Suef University, Beni-Suef 62511, Egypt

Received: 22 May 2023

Accepted: 22 July 2023

Published online:

8 August 2023

© The Author(s) 2023

ABSTRACT

Significant research is being performed to find suitable electrocatalysts in alkaline direct methanol fuel cells. Despite tremendous improvements, producing non-Pt catalysts with great activity and high stability is still difficult. Herein, Ag-doped NiO thin films were deposited on fluorine-doped tin oxide (FTO) by the co-sputtering deposition method, utilizing various deposition times (200, 400, 600, and 800) seconds. The film thickness for the deposited films varied from 17, 35, 70, and 100 nm by increasing the deposition time from 200, 400, 600, to 800) seconds. The NiO–Ag-800 recorded the lowest band gap of 3.36 eV, whereas the NiO–Ag-200 recorded the highest band gap of 3.81 eV. The deposited thin films were used as electrocatalysts for methanol oxidation. Its physical properties facilitate the adsorbed reactions, allow for easier penetration of electrolytes, and help in rapid reaction kinetics. Moreover, because Ag–NiO is deposited on an FTO substrate with outstanding adhesion and excellent electric contact, it can be utilized; without adding any binder or conducting agents. The films displayed reduced onset potential for oxidation of the methanol, high current density, and long-term stability. The thickness of the thin film proved that it plays a role in electroactivity. The efficiency of the films increased with increasing thickness, where the Ag–NiO-800 record the lowest onset potential is 0.37 V vs. Ag/AgCl.

1 Introduction

Due to the great development in technology usage, which depends on electricity, fossil fuels are highly consumed to generate electricity; in addition, It negatively affects the environment [1, 2]. Therefore, researchers focus on developing clean, renewable,

effective, and environmentally acceptable substitute sources to fulfill the expanding required energy demand [3]. Among these sources, direct methanol fuel cells (DMFC), which use methanol as fuel, have become an alternative method of producing electricity [4] as DMFC's offer many advantages like low cost, environmentally friendly, and ease of operation.

Address correspondence to E-mail: mshaabancnt@psas.bsu.edu.eg

Nonetheless, DMFCs have difficulties with methanol crossover, reduced durability, poor stability, trouble controlling heat and water, and high production costs that have rendered their commercialization undesirable [5]. Many researchers have addressed the difficulties of functioning methanol oxidation fuel cells in various cutting-edge ways [6–9]. There are several trials for developing cost-effective and high-performance non-precious electrocatalysts for oxygen reduction reaction (ORR) in acidic and alkaline media, which is an urgent need for clean energy generation [10–14].

The electrocatalyst choice significantly influences the performance of methanol fuel cells [15]. Although platinum and noble-metal-based electrocatalysts are widely utilized in fuel cell applications [16], they are the main reason for the high cost and carbon monoxide poisoning. Hence, researchers turned to electrocatalysts based on non-noble transition metal oxides, demonstrating an efficient strategy for increasing electrocatalytic activity to provide promised alternative catalysts [17]. In particular, NiO_x [18], CoO_x [19], CuO_x [19], CrO_x [20], MnO_x [21], and FeO_x [22] catalysts have demonstrated enhanced reaction kinetics as well as excellent anti-poisoning potential. Ni-based catalysts have been extensively applied in many traditional industrial catalysis processes, including the reforming of methane [23], hydrogenation reactions [24], hydrocracking [24], and oxidation reactions [25] because nickel (Ni) is an economical, abundant, non-precious metal. Furthermore, redox reactions occur on Ni's surface during catalysis, leading to Ni(OH)₂ and NiOOH, considered activity reaction sites of methanol molecules in alkaline electrolytes [26].

Catalysts' morphology and crystalline structure significantly impact their catalytic activity [2]. Nanotechnology has been proven useful in developing more efficient catalysts [1]. Different nanostructures of Ni-based materials have been synthesized with a variety of techniques, including atomic layer deposition [27], sol-gel chemical deposition [28], Spray pyrolysis [29], and hydrothermal processes [30]. Despite considerable improvement, most manufacturing processes must be simplified for industrial use or require chemicals impairing catalyst performance [31]. Furthermore, many Ni-based catalysts suffer from poor long-term durability due to phase transition, structural disintegration, and poor adherence between the catalyst and the conducting substrate,

causing materials loss [32]. Because nickel oxide is highly soluble in most typical alkaline electrolytes, it is challenging to retain enough control over the structure and morphology of the material [33].

Doping can boost electrochemical activity even further because it affects the electronic structure, a critical factor in enhancing electrocatalytic activity. In addition, adding impurities can create ionizable atoms inside the received material [34, 35]. Many elements can affect electrocatalytic activity, but every element selected is used to achieve a specific goal. Therefore, Ag's capacity to establish long-term stability in alkaline environments was documented in several studies [36–40].

In this work, Ag-doped NiO thin films were deposited on FTO substrates via a co-sputtering deposition method and were used as electrocatalysts toward methanol electro-oxidation. To our knowledge, work has yet to be reported on using such a material in its thin film structure as an electrocatalyst for methanol oxidation. The prepared Ag-doped NiO films were composed of a rough surface and suitable thickness because of lengthening the deposition period, facilitating electrolyte adsorption, leading to larger ions diffusion, and providing different active sites. Because Ag-doped NiO films are grown on a substrate with strong adherence like FTO, the Ag-doped NiO can be utilized directly as an electrocatalyst for methanol oxidation without the requirement to add any conducting agent or binder.

2 Materials and methods

2.1 Sample preparation

The co-sputtering deposition method is one of the most important approaches for tuning and monitoring the amount of doping atoms in the hosting thin films. We were able to deposit 3.53% Ag-doped NiO thin films on both glass slides and fluorine-doped tin oxide (FTO) with different thicknesses of 17, 35, 70, and 100 nm by varying deposition times from 200, 400, 600 to 800 s using a DC/RF sputtering equipment (Syskey Technologies, Taiwan). Before the deposition process, the glass slides and FTO were cleaned by acetone and ethanol then dried with nitrogen gas. The DC power for the Ni target was kept at 200 W, while the RF power for the Ag target was kept at 20 W during the sample preparations.

The other deposition parameters are kept constant during the deposition process, like operating pressure, substrate temperature, substrate rotation, oxygen flow rate, and argon flow rate to be 5×10^{-3} Torr, 25 °C, 15 rpm, 10 SCCM, 20 SCCM, respectively. The final samples were named NiO–Ag-200, NiO–Ag-400, NiO–Ag-600, and NiO–Ag-800 based on the deposition times.

2.2 Characterizations of the prepared thin films

X-ray diffraction (Shimadzu LabX-XRD-6000, Japan) at 40 kV/40 mA with Cu–K α radiation (0.154056 nm) is utilized to determine the crystalline phases of thin films. Field emission scanning electron microscopy was used to examine the morphologies and structure (FESEM, Zeiss sigma 500 VP, Germany). The energy-dispersive X-ray fixed on the FESEM was also used to evaluate the elemental makeup and map the components on the film's surface. The optical characteristics of the produced films were characterized using a UV–Vis spectrophotometer (Perkin Elmer Lambda 750; Massachusetts, USA). XPS recorded the chemical state of the prepared thin films collected on K-ALPHA (Thermo Fisher Scientific, USA) with monochromatic X-ray Al K-alpha radiation – 10 to 1350 eV spot size 400 μm at pressure 10^{-9} mbar with full spectrum pass energy 200 eV and at narrow spectrum 50 eV.

2.3 Electrochemical measurements

The electrocatalytic activity of each prepared thin film toward methanol oxidation in an alkaline solution was studied and evaluated by a setup consisting of three electrodes at room temperature. The reference and counter electrodes were Ag/AgCl and Pt wire, respectively, with the synthesized films as working electrodes. In addition, the electrolyte solution contained 0.5 M KOH, with different methanol concentrations utilized (0.5, 1, 2 M). The electrocatalytic activity was evaluated in a pure 0.5 M KOH solution and in the presence of methanol by combining the estimated volume of methanol with the KOH solution. An Autolab PGSTAT302N potentiostat (Metrohm) was used for all electrochemical experiments, using cyclic voltammetry (CV) at scan rates ranging from 5 to 100 mV s^{-1} , chronoamperometry (CA) at 0.6 V for 1 h and electrochemical

impedance spectroscopy (EIS) at 0.6 V with an amplitude of 10 mHz. The current densities have been standardized based on the electrodes' geometric surface area.

3 Results and discussion

3.1 Structural analysis

The crystallinity of all produced films is analyzed by XRD, as shown in Fig. 1. The ICDD Card [01-089-3080] matched the diffraction peaks, identifying the space group R-3 m (166) of a single phase of trigonal-structured nickel oxide. Due to the minimal quantity of Ag added to nickel oxide, no other peaks distinct from those found in pure nickel oxide (021), (202), and (220) formed. The XRD data demonstrates that the NiO films are perfectly crystalline and have a high purity level.

The mean crystallite size D was calculated using the Debye Scherrer Eqs. [41, 42].

$$D = \frac{0.94 \lambda}{\beta \cos \theta} \quad (1)$$

where D is crystallite size, λ is the used wavelength of the X-ray, β the Full width at half maximum (FWHM) of the peak, and θ is the diffraction angle.

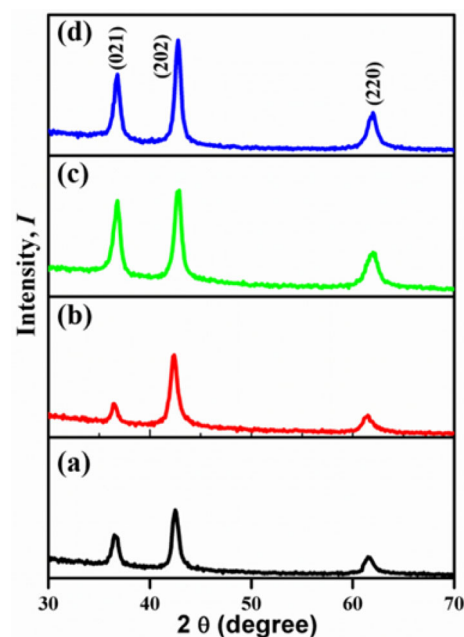


Fig. 1 X-ray diffraction of NiO–Ag thin films deposited by different time **a** 200, **b** 400, **c** 600, **d** 800s

Also, the following formula (2) and (3) were used to compute dislocation density δ and lattice strain [35, 43].

$$\delta = \frac{n}{D^2} \quad (2)$$

$$\varepsilon = \frac{\beta \cos \theta}{4} \quad (3)$$

Table 1 displays the structural attributes of produced films of different thicknesses, including average crystallite size, dislocation density, and lattice strain. The results show that an increase in deposition time has a relative impact on crystallite size for the films, with NiO–Ag 800 having the largest size at 10.93 nm and NiO–Ag 200 having 9.41 nm. Since the content of Ag in NiO–Ag thin films is very low, the positions of the three diffraction peaks are very close to those of pure NiO previously presented in the literature [44]. The deposition time effect is not clear on the crystallinity of the prepared films; this is maybe due to the chemical composition being the same in all samples, and the only difference is the thickness. However, with increasing the deposition time, there is a clear change in the microstructure of the prepared films where the sample's surface becomes rougher in the case of thicker samples. In addition, a porous structure configuration appeared with increasing the sample thickness, which is favorable for fast ion/electron transport and

enhanced electrochemical reactivity toward methanol electrooxidation.

3.2 X-ray photoelectron spectroscopy

The shift in core-level binding energies in the XPS spectrum can be used to determine the oxidation states of NiO–Ag. Figure 2a depicts the NiO–Ag-800 composite films' XPS survey spectrum. The C 1s, O 1s, Ag 3d_{3/2}, and Ni 2p_{3/2} spectral lines are responsible for the peaks in the spectrum, which were prominently seen at their respective standard binding energies of 284.3, 529.6, 368.5, and 855.2 eV. The strong peak at 855.2 eV, a characteristic peak of the NiO phase, is shown by the NiO–Ag-800 sample. Ni 2p_{3/2} and 2p_{1/2} have core-level binding energies of 854.8 and 872.3 eV, respectively, as shown in Fig. 2b.

The Ni 2p deconvolution spectrum is depicted in Fig. 2b as two-component peaks, Ni⁺² (NiO) and Ni⁺³ (Ni₂O₃), respectively [45, 46]. The curves show the deconvolution resulting from NiO (853.2 eV) and Ni₂O₃ (855.6 eV), two separate components of nickel oxide films. Additionally, there is a very broad peak at 861.3 eV, which is the Ni⁺² and Ni⁺³ shake-up satellite peak. The nickel oxide peak-corresponding Gaussian curves were used to match the XPS spectra. These findings agreed with earlier studies of the composition and chemical states of Ni 2p_{3/2} in nickel oxide thin films created by reactive magnetron sputtering [47–49].

Table 1 The structural characteristics of the prepared thin films

Material	2 θ ^o	(hkl)	Crystallite size, (nm)	Dislocation density	Lattice strain
NiO–Ag-200	36.76	(021)	10.65	8.81E–03	3.25E–03
	42.81	(202)	10.89	8.43E–03	3.18E–03
	61.92	(220)	6.71	2.22E–02	5.16E–03
Mean value			9.41	1.31E–02	3.86E–03
NiO–Ag-400	36.61	(021)	10.87	8.46E–03	3.19E–03
	42.46	(202)	11.84	7.13E–03	2.93E–03
	61.44	(220)	8.64	1.34E–02	4.01E–03
Mean value			10.45	9.66E–03	3.37E–03
NiO–Ag-600	36.40	(021)	13.57	5.43E–03	2.55E–03
	42.38	(202)	10.47	9.12E–03	3.31E–03
	61.27	(220)	7.52	1.77E–02	4.61E–03
Mean value			10.52	1.07E–02	3.49E–03
NiO–Ag-800	36.72	(021)	11.63	7.39E–03	2.98E–03
	42.76	(202)	12.76	6.14E–03	2.72E–03
	61.87	(220)	8.42	1.41E–02	4.11E–03
Mean value			10.93	9.21E–03	3.27E–03

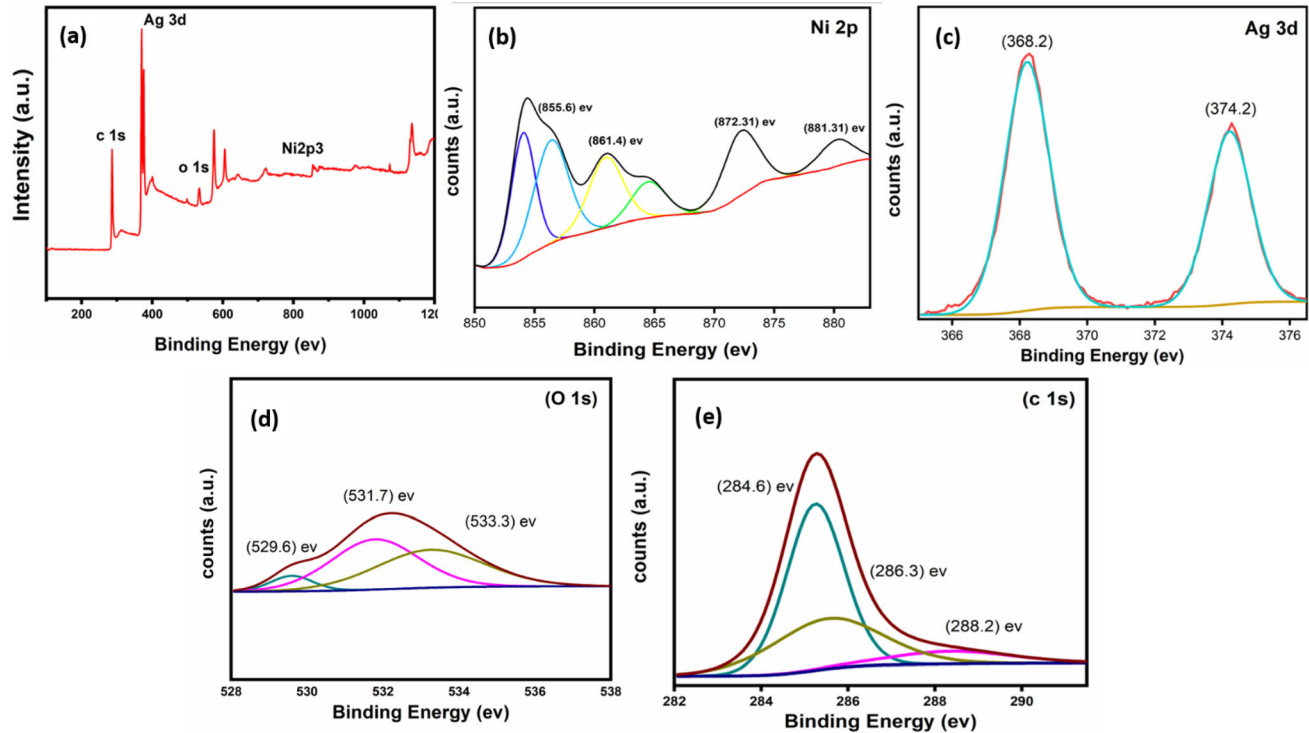


Fig. 2 XPS spectra of NiO–Ag 800, **a** survey spectra, **b** Ni 2p, **c** Ag 3d, **d** O 1s and **e** C 1s spectra

The narrow scan XPS spectra of Ag 3d core-level binding energy are displayed in Fig. 2c. Ag 3d_{5/2} and Ag 3d_{3/2} were connected to the core-level binding energies of 368.2 and 374.2 eV, respectively [50]. The lower energy peak at 368.2 eV was attributed to Ag metal in the films, and the peak at 374.2 eV was attributed to Ag at Ni substitutional sites in the NiO matrix. By carefully comparing those peak heights in the spectrum with the presumption that Ag composition was uniform at the surface region, it is possible to determine the composition at the near-surface region. The absence of the Ag-related phase in the XRD results while the surface presence of Ag ions was seen by XPS suggested that the Ag ions were oxidized in the NiO matrix.

The deconvolution of the O1s photoelectron signal for NiO–Ag films is depicted in Fig. 2d. Analysis of the NiO–Ag films oxygen's 1s line reveals the presence of oxygen atoms coming from the M–O peak (529.6 eV binding energy) and OH peak (531.7 eV binding energy), whereas the peaks at 533.3 eV are caused by absorbed water or other oxygen-containing species like OH or CO on the thin film's surface. This demonstrates how the surface instability of the material increases with the amount of oxygen present. In the XPS data, the OH phase is present to a

lesser extent than the oxygen state I (O 1s). The XRD measurement did not reveal it. Figure 2e presents peaks with 286.3 and 288.2 eV binding energies assigned to the O–C–O oxygen-containing carbonaceous band and the C–O, respectively. And the C–C bond is identified by the deconvoluted peak with a binding energy of 284.6 eV [51]. All of the deposited films were found to be single phases of NiO–Ag composites, according to the XPS investigations.

3.3 Morphological analysis

FESEM images of all thin films NiO–Ag with varying deposition periods (200, 400, 600, and 800 s) are shown in Fig. 3. The images demonstrate how the films were rougher by lengthening the deposition period and displaying more particle agglomerations. The grain particles in the morphology are not uniform in size; it is also obvious that the synthesized films have defect. EDS was used to evaluate the elemental analyses of deposited films NiO–Ag-200 as shown in Fig. 4d; the spectra for the elements Ni, O, and Ag are clearly observed, which confirms the purity of the deposited NiO–Ag thin films, this result agrees with the results obtained by XPS. The EDS

Fig. 3 FESEM images of NiO–Ag thin films deposited for **a** 200, **b** 400, **c** 600, **d** 800 s

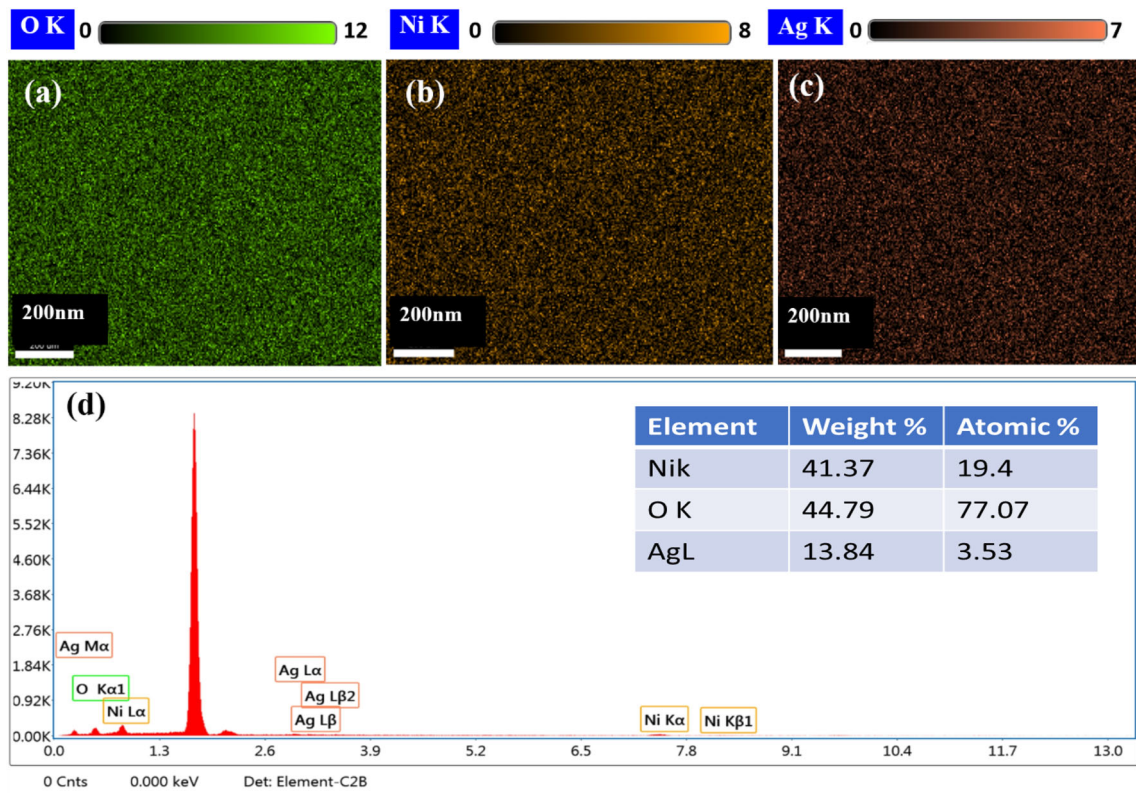
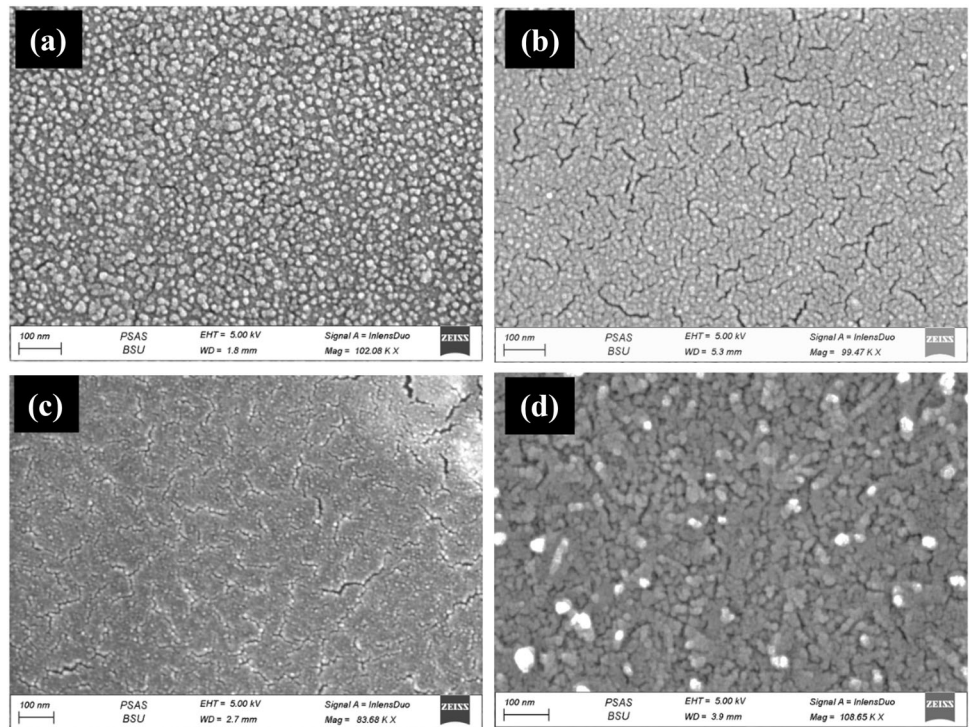


Fig. 4 EDS spectrum of NiO–Ag 200, **a** O, **b** Ni, **c** Ag, and **d** Elemental mapping images of Ni, O, and Ag

mapping also confirm the homogeneous distribution of different elements (Ni, O, and Ag) over the surface of the FTO substrate, as clear in Fig. 4a–c.

SEM images were captured with a 45-degree tilt to define how deposition time affected the resulting film thickness (see Fig. 5). It is obvious that extending the deposition period during preparation increases the thin film thickness. The thickness of NiO–Ag-200 is around 17 nm (Fig. 5a), whereas that of NiO–Ag-800 film is approximately 100 nm (Fig. 5d), increasing by a factor of five.

3.4 Optical analysis

The analyses of optical transmittance by UV–vis spectroscopy are shown in Fig. 6. With increasing layer thickness; there is a significant and anticipated drop in transmittance, which may be caused by simpler charge transfer. Moreover, the bandgap of films was calculated using the Tauc relation, as shown in Eq. [52–54].

$$\alpha = \frac{A}{h\nu} (h\nu - E_g)^n \tag{4}$$

where A is a constant, h is the photon’s energy that was incident, and (α) is the absorbance coefficient. According to the quantum selection principles for

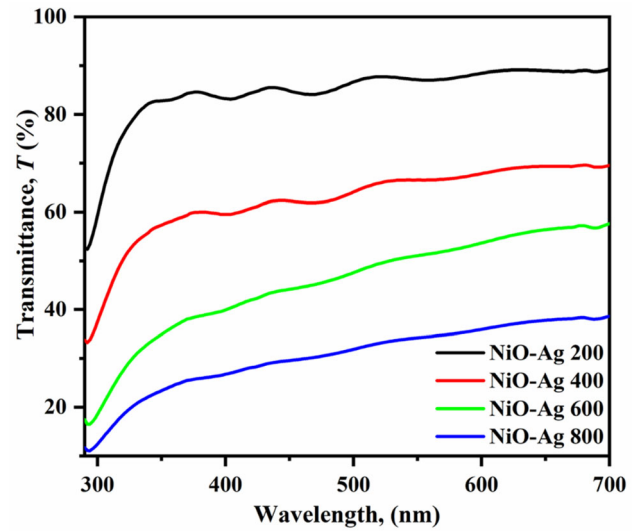
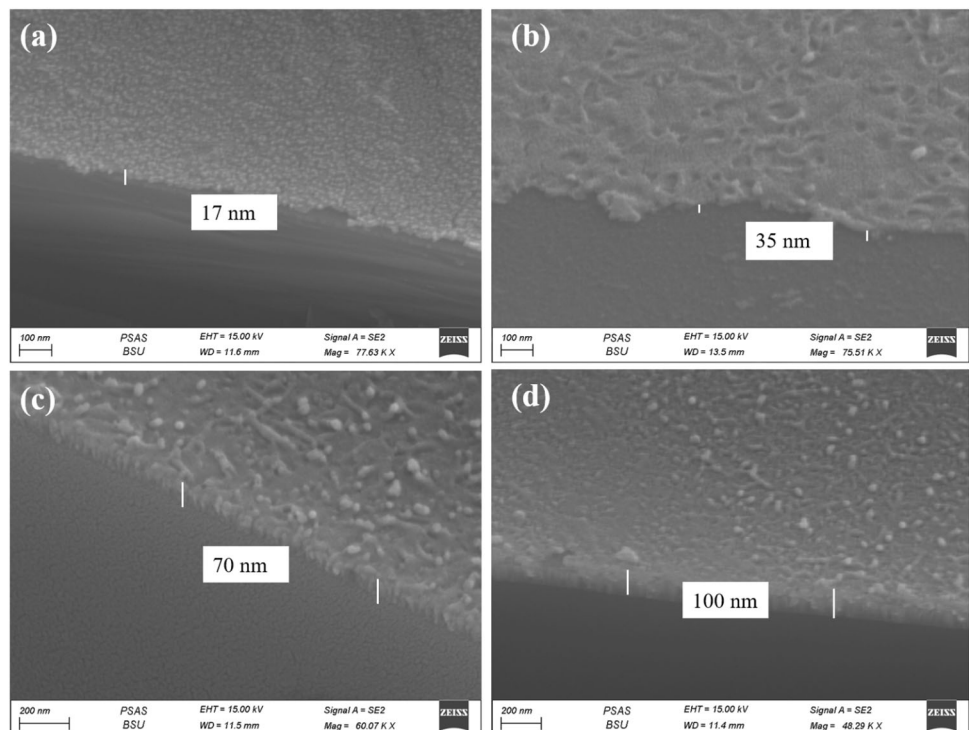


Fig. 6 Optical transmittance of the prepared thin films

different materials, (n) may equal 1/2 or 2 for the direct and indirect band gaps, respectively.

The band gaps of the films were evaluated by the intersection of the linear areas and the photon energy $(h\nu)$ axis. Figure 7 shows the effect of the thickness on the band gap values; the NiO–Ag-800 recorded the lowest band gap of 3.36 eV, whereas the NiO–Ag-200 recorded the highest band gap of 3.81 eV. The cause might be related to enhancements in crystallinity, as

Fig. 5 Thickness of the thin films is presented by FESEM of NiO–Ag a 200, b 400, c 600, d 800



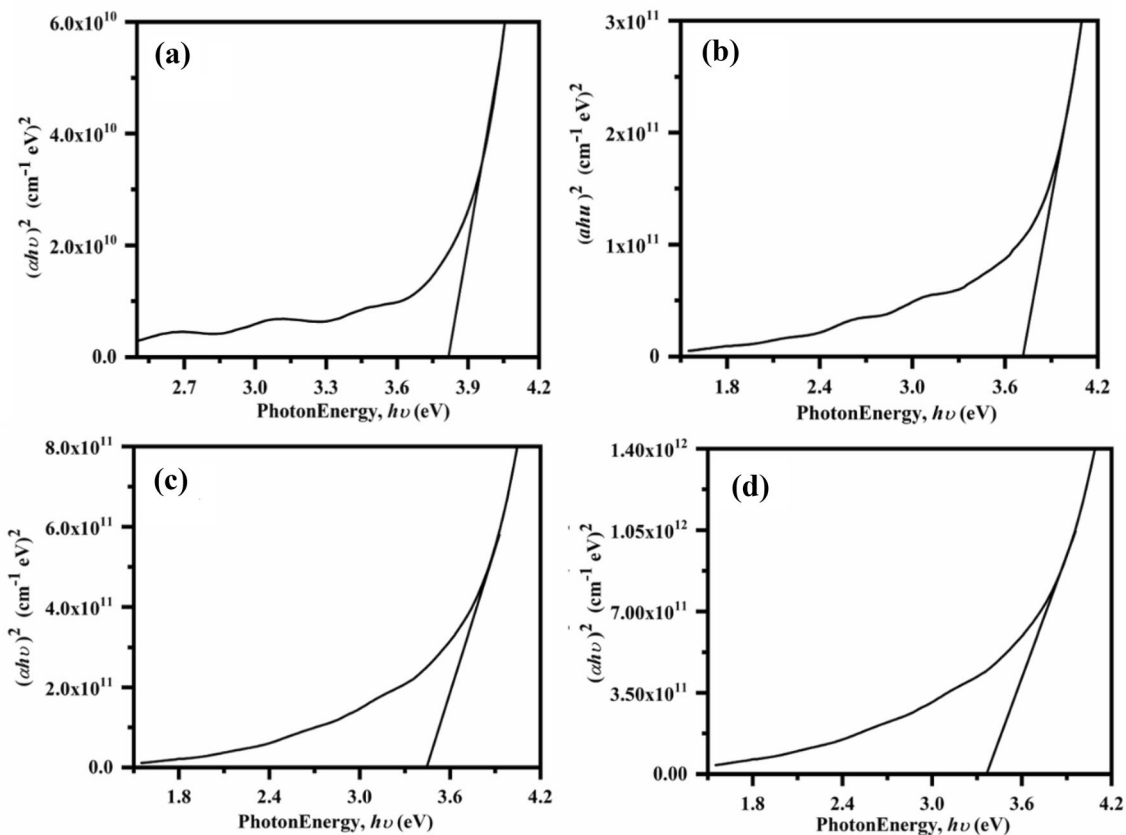


Fig. 7 Optical band gaps of the prepared thin films

described above in the XRD and FESEM; also, some research suggests that when the thickness of the film increase, the localized states in the band structure may overlap with the band boundaries, minimizing the band gap [36, 37].

3.5 Electrocatalytic activity

The CV curves of all films in 0.5 M KOH electrolyte at various scan rates (5, 10, 20, 30, 50, and 100 mV s^{-1}) vs. Ag/AgCl throughout a potential window of 0–0.6 V at ambient temperature are shown in Fig. 8 There are pair peaks (oxidation and reduction) in the anodic and cathodic sweeps associated with $\text{Ni}^{2+}/\text{Ni}^{3+}$ activation. Ni and Ag species provide two electroactive centers to enrich the redox processes, which can improve the oxidation process simultaneously. The anodic and cathodic current densities have grown with an increase in deposited time due to the thickness of films, which contains a larger quantity of Ni and Ag, increasing the active sites. Suggested that the more active sites are exposed on the thicker sample based on the courser surface as cleared from

SEM images, maybe there is a secondary electron transfer that is at play.

The linear relationship between the anodic and cathodic current densities and the square root of the scan rate (5–100 mV/s) is displayed in Fig. 9 for each film. According to the results, increasing scan speed causes an increase in the oxidation-reduction reaction, and OH^- migration into the pores' cavities improves the electrochemical process [55]. It is evident from Figs. (8 and 9) that NiO–Ag-800 outperforms other materials in redox reactions at various scan rates because it has a significant amount of Ni^{2+} , Ni^{3+} , and Ag that has been spread out on the FTO surface due to formation of multiple successive layers to increase the thickness. This improves catalytic activity by speeding up the diffusion of OH^- ions onto the surface.

3.6 Electrocatalytic activity toward methanol oxidation

The synthesized thin films were tested for methanol oxidation performance in an alkaline electrolyte

Fig. 8 Cyclic voltammograms for films in 0.5 M KOH at room temperature with various scan rates **a** NiO–Ag-200, **b** NiO–Ag-400, **c** NiO–Ag-600, **d** NiO–Ag-800

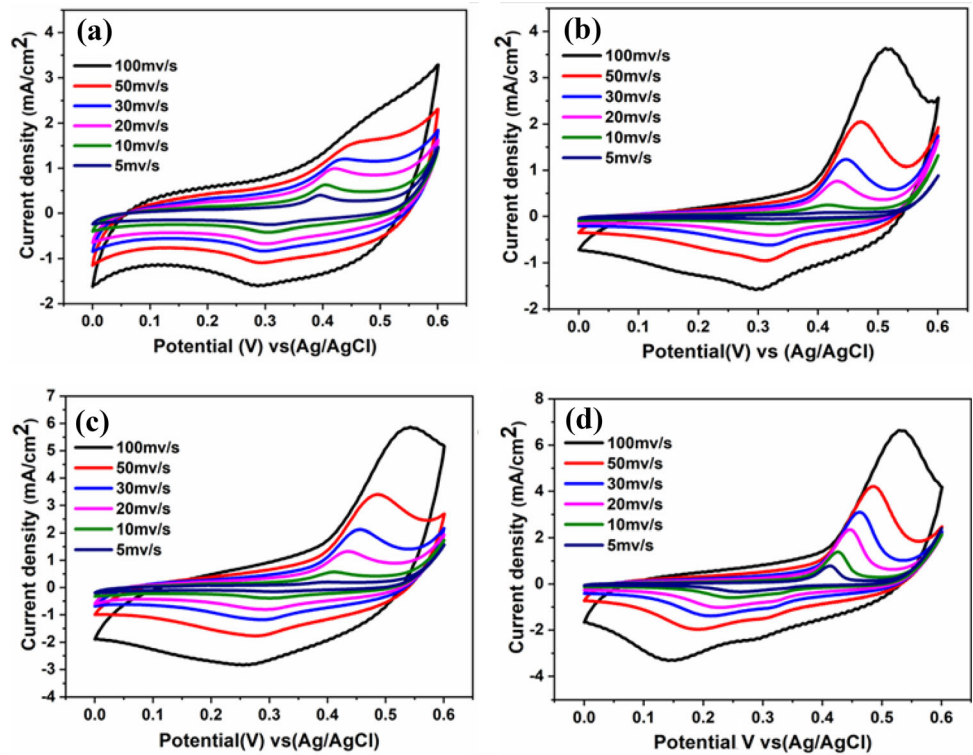


Fig. 9 The relationship between current density with the square root of the scan rate for anode and cathode **a** NiO–Ag-200, **b** NiO–Ag-400, **c** NiO–Ag-600, **d** NiO–Ag-800

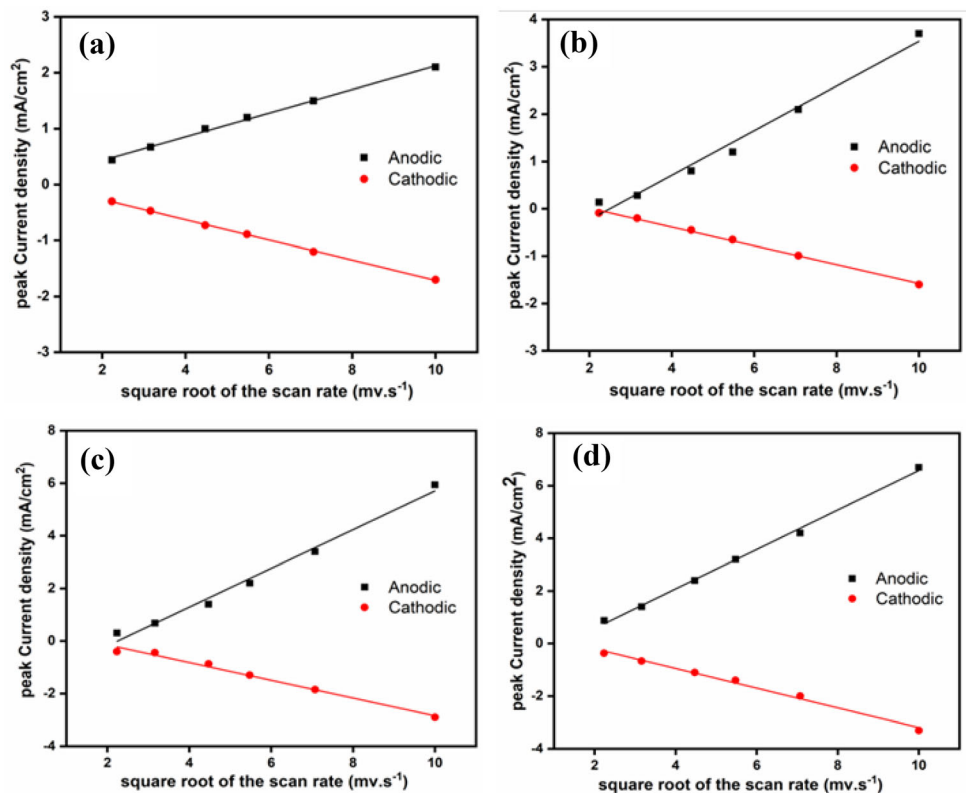


Fig. 10 Cyclic voltammograms of thin films in 0.5 M KOH + 0.5 M methanol solution with a scan rate of 50 mV/s at room temperature **a** NiO–Ag 200 **b** NiO–Ag 400 **c** NiO–Ag 600 **d** NiO–Ag 800

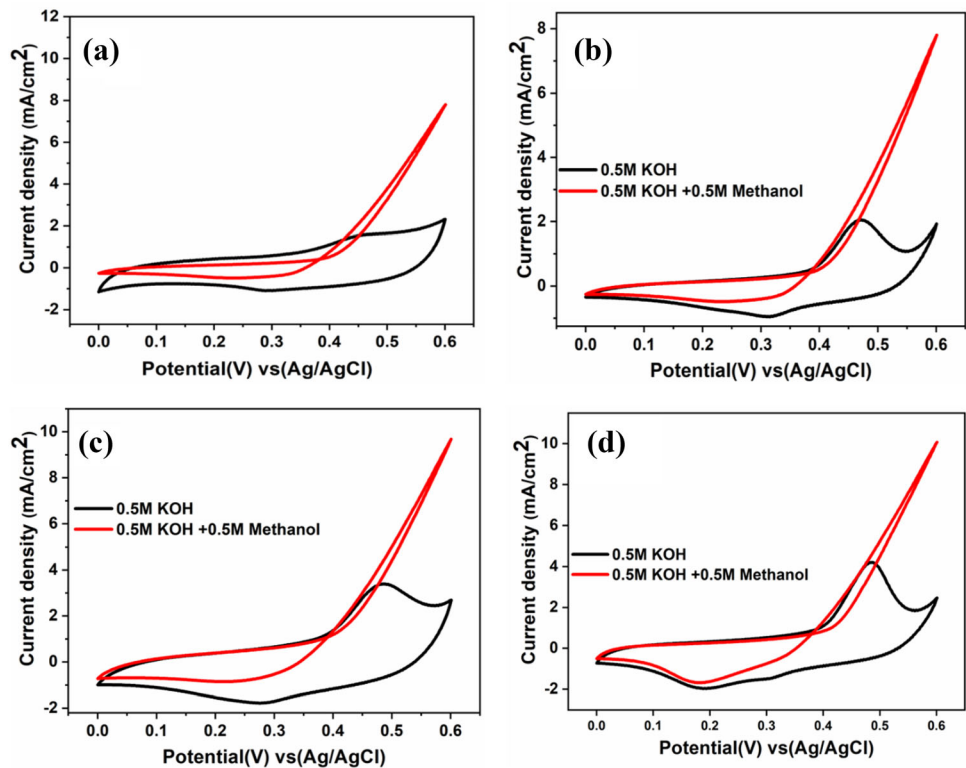
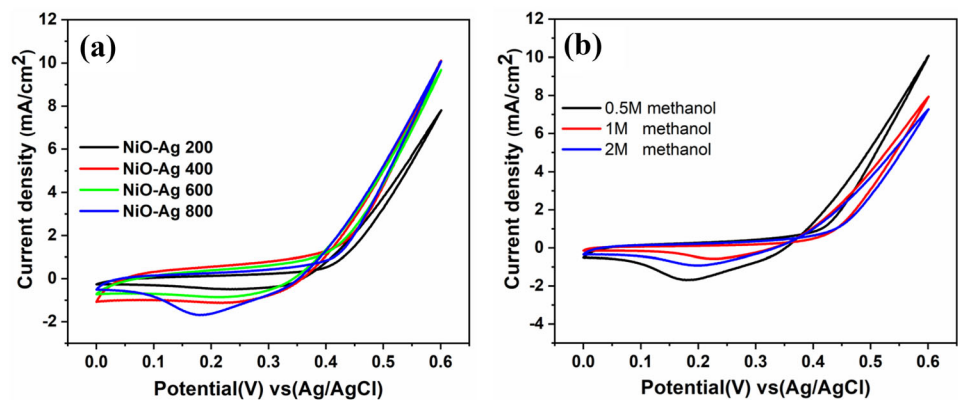


Fig. 11 **a** Cyclic voltammogram of thin films in 0.5 M KOH + 0.5 M methanol solution at scan rate 50 mV s⁻¹ at room temperature, **b** CVs at different concentrations of methanol at scan rate 50 mV/s for Ag–NiO 800



(0.5 M KOH) mixed with 0.5 M methanol at 50 mV s⁻¹ scan rate as shown in Fig. 10. Ag/AgCl was used as a reference electrode, and the platinum a counter electrode. Two crucial variables for describing the electrochemical characteristics of any electrocatalyst are current density and onset potential. The current density increases with increasing the films thickness NiO–Ag-800 NiO–Ag-600, NiO–Ag-400, and NiO–Ag-200 recorded 10.5, 10, 9, 8 mA cm⁻², respectively, as presented in Fig. 11a, the reason is due to the long deposited period, as the amount of deposited material increased, which led to

an increase Ni and Ag, which are the activity sites for methanol oxidation as reported in the mechanism [56]. Moreover, the onset potential doesn't change, recording 0.37 V. This is normal because ratios are constant between the elements as confirmed by EDX results. The good activity for films toward methanol oxidation is due to the good crystallite shown above by XRD [57]. Additionally, the 2 D structures (thin film shape) play an important role in exposing large surfaces and increasing the films' active area to reactions. These results are very promising if we compare them with some previously reported

Table 2 MOR performance of NiO–Ag-800 film compared to Ni-based electrocatalysts

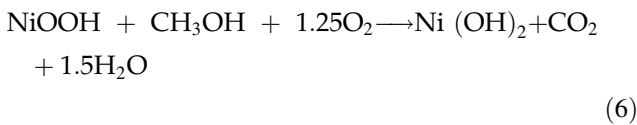
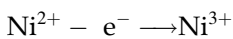
Catalysts	Methods of preparation	Morphology	Current density (mA cm ⁻²)	Onset potential	References
NiO–Ag 800	Co-sputtering deposition	Thin film	10.5	0.37	This work
Ni/ZIF-8	Mixed under stirring	Nanoparticles	0.74	0.75	[58]
NiO	Hydrothermal	Nanosheet	9.5	0.5	[59]
NiO	Hydrothermal	Nanoflake	1.9	0.87	[60]
GC/NiO _x	Potentiostatic deposition	Nanoparticles	0.5	0.44	[61]
NiMoO ₄	Hydrothermal	Nanorod	2.5	0.45	[62]
Fe–Ni	Laser irradiation	Nanoparticles	8	1.4	[63]

catalysts, as shown in Table 2. NiO–Ag-800 is tested at different concentrations of methanol (0.5, 1, and 2 M), however the best results were in 0.5 M methanol, as presented in Fig. 11b.

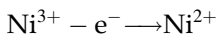
The mechanism of NiO for methanol oxidation is described by many articles [64–67].



Or



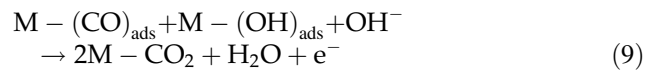
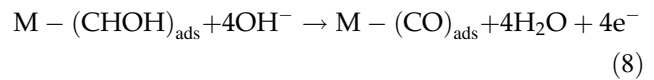
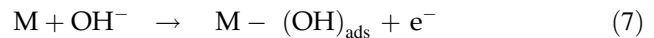
Or



NiO–Ag films adsorbed the methanol molecule from the electrolyte media by electrocatalytic active sites provided with (Ni⁺² and Ni⁺³) redox pair and Ag. Therefore, the CO intermediates are left on the electrocatalyst’s surface after the absorbed MeOH

undergoes electro-oxidation, then OH⁻ ions are adsorbed from supporting electrolytes onto the trap centers of the NiO films. Finally, the CO oxide is into CO₂ by the adsorbed OH molecules, restoring electroactive sites and enhancing long-term stability [68].

Figure 12a displays electrochemical impedance measurements at a frequency range from (0.01 to 100,000) Hz using film with 1 cm² area at 0.6 V vs. Ag/Ag Cl in 0.5 M KOH containing 0.5 M methanol. According to the mechanism of MOR in alkaline media, there are several steps, as appear in the following equations:



where M acts as an active site on the electrode’s surface.

The mechanism begins with hydroxyl ion oxidative adsorption in Eq. 7. Then adsorbed carbon monoxide

Fig. 12 a Nyquist plots for the oxidation reaction, b Thin films stability, at 0.60 V using 0.5 M methanol

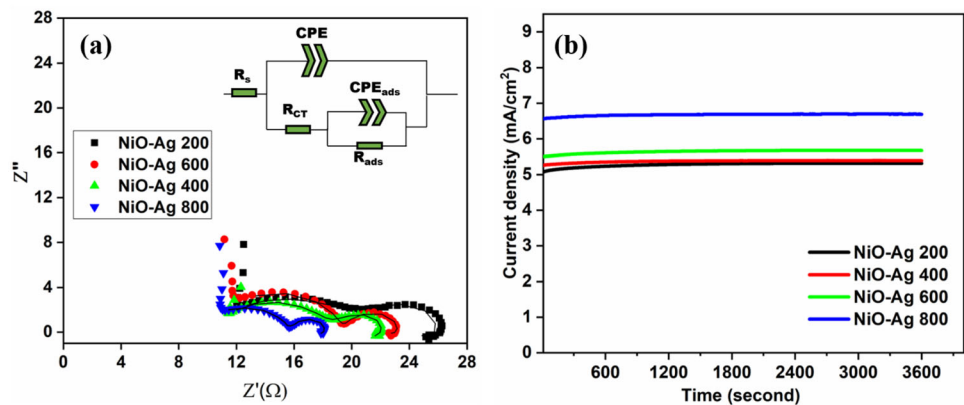


Table 3 EIS values fitted by the equivalent circuit

The prepared films	R_s	CPE		R_{ct}	C_{ads}		R_{ads}
		CPE T	CPE P		CPE T	CPE P	
NiO–Ag 200	9.38	4E–04	0.55	12.49	2E–03	1.04	3.78
NiO–Ag 400	9.51	3.2E–04	0.61	10.12	5.2E–03	1.00	3.33
NiO–Ag 600	9.8	2.2 E–04	0.64	9.42	7.5E–03	1.00	2.74
NiO–Ag 800	9.1	1.2 E–04	0.66	7.33	12.3E–02	1.00	2.05

is produced through dehydrogenation and oxidative adsorption of methanol as shown in Eq. 8. Consequently, Eq. 9 demonstrates how to make carbon dioxide and replenish active catalytic sites. All thin films generally exhibit a small semicircle diameter not exceeding 26 ohms, including the electrolyte's resistance. It is observed that the EIS decreases with an increase in the thickness of deposited thin films on FTO because the intensity of ions increased, leading to enhanced charge transfer kinetics throughout the MOR process.

The EIS data were fitted utilizing the equivalent circuit illustrated inside of Fig. 12a. where the R_s is the electrolyte's resistance, CPE is the constant phase element, and R_{ct} is the charge transfer resistance. At the same time, C_{ads} and R_{ads} are the elements associated with intermediate reaction adsorption, according to Table 3. R_{ads} for NiO–Ag films are very low, implying rapid kinetic of methanol oxidation and simpler methanol adsorption.

Figure 12b shows the long-term stabilities activities of films evaluated by chronoamperometry testing at a constant voltage of 0.6 V for 1 h. It is observed that there is no decay of initial current density values to the end of the period time, referring to strong stability for all electrodes. Most electrocatalysts for methanol oxidation (MOR), even the precious and commercially available Pt, are not long-lasting because of the buildup of carbonaceous reaction intermediates like CO on the surface of the electrode. Therefore, the long-term stability test is a crucial examination and important for excellent electrocatalysts.

4 Conclusion

NiO–Ag films were successfully synthesized through a simple physical vapor deposition approach by co-sputtering deposition. This method possesses many advantages to fabricated films to be excellently

qualified as electrocatalysts in methanol oxidation, such as small crystallites that are uniformly dispersed and have a high specific surface area. Therefore, the good distribution of elements over the surface of the FTO substrate, confirmed by EDS, led to increased electroactive sites, helping the Ag-doped NiO act as an effective electrocatalyst for MOR as appeared by electrochemical measurements because of accelerated reaction kinetics and enhanced ion diffusion. Moreover, the results show that the electroactivity of films increases with increased thickness, where the Ag–NiO-800 record the lowest onset potential is 0.37 V vs. Ag/AgCl. All films displayed great stability according to the preparation method of Ag–NiO films are grown on a metallic substrate to increase the adhesion and used as electrocatalysts directly for MOR without adding any binder or conducting agents.

Acknowledgements

Not applicable.

Author contributions

MSh.Aw: Methodology, Conceptualization, Data curation, Visualization, Investigation, Writing—reviewing & editing. HK.EE: Methodology, Software, Validation, Writing—original draft. WMAER: Methodology, Conceptualization, Data curation Supervision, Writing—reviewing & editing. All authors contribute to the revisions of the manuscript in its final form and agree to the submission.

Funding

Open access funding provided by The Science, Technology & Innovation Funding Authority (STDF)

in cooperation with The Egyptian Knowledge Bank (EKB). Open access funding provided by The Science, Technology & Innovation Funding Authority (STDF) in cooperation with The Egyptian Knowledge Bank (EKB). No funds were received.

Data availability

The data and materials that support the findings of this study are available from the corresponding author upon reasonable request.

Declarations

Conflict of interest The authors declare that they have no conflict of interest.

Ethics approval All authors approved the submission.

Consent to participate All authors approved the submission.

Consent for publication All authors approved the submission.

Open Access This article is licensed under a Creative Commons Attribution 4.0 International License, which permits use, sharing, adaptation, distribution and reproduction in any medium or format, as long as you give appropriate credit to the original author(s) and the source, provide a link to the Creative Commons licence, and indicate if changes were made. The images or other third party material in this article are included in the article's Creative Commons licence, unless indicated otherwise in a credit line to the material. If material is not included in the article's Creative Commons licence and your intended use is not permitted by statutory regulation or exceeds the permitted use, you will need to obtain permission directly from the copyright holder. To view a copy of this licence, visit <http://creativecommons.org/licenses/by/4.0/>.

References

1. N. Ahmed, A.A. Farghali, W.M.A. El Rouby, N.K. Allam, *Int. J. Hydrogen Energy*. **42**, 29131 (2017)
2. H. El Emam, S.I. El-Dek, W.M.A. El Rouby, *J. Electrochem. Soc.* **168**, 050540 (2021)
3. S. Gamil, W.M.A. El Rouby, M. Antuch, I.T. Zedan, *RSC Adv.* **9**, 13503 (2019)
4. S. Sakong, A. Groß, *ACS Catal.* **6**, 5575 (2016)
5. A.F. Carley, A.W. Owens, M.K. Rajumon, M.W. Roberts, S.D. Jackson, *Catal. Lett.* **37**, 79 (1996)
6. H.M. Villullas, F.I. Mattos-Costa, L.O.S. Bulhões, *J. Phys. Chem. B* **108**, 12898 (2004)
7. J. Xu, X. Liu, Y. Chen, Y. Zhou, T. Lu, Y. Tang, *J. Mater. Chem.* **22**, 23659 (2012)
8. M.B. Askari, P. Salarizadeh, M. Seifi, S.M. Rozati, *Solid State Sci.* **97**, 1 (2019)
9. R.M.A. Tehrani, S. AbGhani, *Fuel Cells*. **9**, 579 (2009)
10. A. Bala Musa, M. Tabish, A. Kumar, M. Selvaraj, M. Abubaker Khan, B.M. Al-Shehri, M. Arif, M. Asim Mushtaq, S. Ibraheem, Y. Slimani, S. Ajmal, T. Anh, Nguyen, G. Yasin, *Chem. Eng. J.* **451**, 138684 (2023)
11. S. Ajmal, A. Kumar, M. Tabish, M. Selvaraj, M.M. Alam, M.A. Mushtaq, J. Zhao, K.A. Owusu, A. Saad, M. Tariq, G. Yasin, *Mater. Today* (2023). <https://doi.org/10.1016/j.mattod.2023.05.022>
12. G. Yasin, S. Ibrahim, S. Ajmal, S. Ibraheem, S. Ali, A.K. Nadda, G. Zhang, J. Kaur, T. Maiyalagan, R.K. Gupta, A. Kumar, *Coord. Chem. Rev.* **469**, 214669 (2022)
13. G. Yasin, S. Ali, S. Ibraheem, A. Kumar, M. Tabish, M.A. Mushtaq, S. Ajmal, M. Arif, M.A. Khan, A. Saad, L. Qiao, W. Zhao, *ACS Catal.* **13**, 2313 (2023)
14. A. Kumar, G. Yasin, M. Tabish, D. Kumar Das, S. Ajmal, A. Kumar Nadda, G. Zhang, T. Maiyalagan, A. Saad, R.K. Gupta, M.M. Makhoulouf, S. Ibraheem, *Chem. Eng. J.* **445**, 136784 (2022)
15. R.P. O'Hayre, *EPJ Web. Conf.* **148**, 1 (2017)
16. E.H. Yu, K. Scott, R.W. Reeve, *J. Electroanal. Chem.* **547**, 17 (2003)
17. W. Huang, H. Wang, J. Zhou, J. Wang, P.N. Duchesne, D. Muir, P. Zhang, N. Han, F. Zhao, M. Zeng, J. Zhong, C. Jin, Y. Li, S.T. Lee, H. Dai, *Nat. Commun.* **6**, 1 (2015)
18. T.J. Wang, H. Huang, X.R. Wu, H.C. Yao, F.M. Li, P. Chen, P.J. Jin, Z.W. Deng, Y. Chen, *Nanoscale*. **11**, 19783 (2019)
19. S. Zafeiratos, T. Dintzer, D. Teschner, R. Blume, M. Hävecker, A. Knop-Gericke, R. Schlögl, *J. Catal.* **269**, 309 (2010)
20. Y. Chen, I.E. Wachs, *J. Catal.* **217**, 468 (2003)
21. H. Huang, X. Wang, *Phys. Chem. Chem. Phys.* **15**, 10367 (2013)
22. T. Noor, M. Mohtashim, N. Iqbal, S.R. Naqvi, N. Zaman, L. Rasheed, M. Yousuf, *J. Electroanal. Chem.* **890**, 115249 (2021)

23. D. San-José-Alonso, J. Juan-Juan, M.J. Illán-Gómez, M.C. Román-Martínez, *Appl. Catal. A Gen.* **371**, 54 (2009)
24. Y.G. Wu, M. Wen, Q.S. Wu, H. Fang, *J. Phys. Chem. C* **118**, 6307 (2014)
25. L. Han, S. Dong, E. Wang, *Adv. Mater.* **28**, 9266 (2016)
26. A.A. Al-Ghamdi, M.S. Abdel-Wahab, A.A. Farghali, P.M.Z. Hasan, *Mater. Res. Bull.* **75**, 71 (2016)
27. W.-H. Kim, H.-B.-R. Lee, K. Heo, Y.K. Lee, T.-M. Chung, C.G. Kim, S. Hong, J. Heo, H. Kim, *J. Electrochem. Soc.* **158**, D1 (2011)
28. Y. Jiang, S. Yang, Z. Hua, H. Huang, *Angew. Chem. Int. Ed.* **48**, 8529 (2009)
29. R.S. Kate, S.A. Khalate, R.J. Deokate, *J. Anal. Appl. Pyrol.* **125**, 289 (2017)
30. C. Upadhyay, D. Mishra, H.C. Verma, S. Anand, R.P. Das, *J. Magn. Magn. Mater.* **260**, 188 (2003)
31. B. Park, E.J. Cairns, *Electrochem. Commun.* **13**, 75 (2011)
32. Y. Mao, H. Yang, J. Chen, J. Chen, Y. Tong, X. Wang, *Nano Energy.* **6**, 10 (2014)
33. T. Noor, S. Pervaiz, N. Iqbal, H. Nasir, N. Zaman, M. Sharif, E. Pervaiz, *Nanomaterials.* **10**, 1 (2020)
34. S.R. Ede, Z. Luo, *J. Mater. Chem. A Mater.* **9**, 20131 (2021)
35. S.C. Bulakhe, R.J. Deokate, *J. Mater. Sci.: Mater. Electron.* **33**, 18180 (2022)
36. G.E. Shter, H. Behar-Levy, V. Gelman, G.S. Grader, D. Avnir, *Adv. Funct. Mater.* **17**, 913 (2007)
37. H. You, L. Zhao, Y. Zuo, J. Fang, *Part. Part. Syst. Charact.* **39**, 1 (2022)
38. W. Wang, H. Zhang, D. Lin, Z. Tao Xiong, *Appl. Catal. B* **24**, 219 (2000)
39. Y. Aouat, G. Marom, D. Avnir, V. Gelman, G.E. Shter, G.S. Grader, *J. Phys. Chem. C* **117**, 22325 (2013)
40. H. Gharibi, K. Kakaei, M. Zhiani, M.M. Taghiabadi, *Int. J. Hydrogen Energy.* **36**, 13301 (2011)
41. J.S.J. Hargreaves, *Catal. Struct. React.* **2**, 33 (2016)
42. R.S. Kate, S.C. Bulakhe, R.J. Deokate, *J. Electron. Mater.* **48**, 3220 (2019)
43. K. Venkateswarlu, M. Sandhyarani, T.A. Nellaippan, N. Rameshbabu, *Proc. Mater. Sci.* **5**, 212 (2014)
44. M.S. Abdel-Wahab, H.K.E. Emam, W.M.A.E. Roubay, *RSC Adv.* **13**, 10818 (2023)
45. A. Davidson, J.F. Tempere, M. Che, H. Roulet, G. Dufour, *J. Phys. Chem.* **100**, 4919 (1996)
46. C.H. Hager, J. Sanders, S. Sharma, A. Voevodin, A. Segall, *Tribol. Int.* **42**, 491 (2009)
47. D.H. Lee, S.Y. Yoon, D.H. Yoon, S.J. Suh, *J. Korean Phys. Soc.* **44**, 1079 (2004)
48. I. Hotový, J. Huran, J. Janík, A.P. Kobzev, *Vacuum.* **51**, 157 (1998)
49. A.P. Grosvenor, M.C. Biesinger, R.S.C. Smart, N.S. McIntyre, *Surf. Sci.* **600**, 1771 (2006)
50. F.X. Bock, T.M. Christensen, S.B. Rivers, L.D. Doucette, R.J. Lad, *Thin Solid Films.* **468**, 57 (2004)
51. P. Hong, Z. Wu, D. Yang, K. Zhang, J. He, Y. Li, C. Xie, W. Yang, Y. Yang, L. Kong, J. Liu, *Chem. Eng. J.* **421**, 129594 (2021)
52. M.M. Abbas, A. Ab, A.K. Al-Samuraee, N.A. Hassan, *Energy Procedia.* **6**, 241 (2011)
53. M. Ali Yildirim, A. Ateş, *Opt. Commun.* **283**, 1370 (2010)
54. K. Mageshwari, R. Sathyamoorthy, *Mater. Sci. Semicond. Process.* **16**, 337 (2013)
55. A. Zaher, W.M.A. El Roubay, N.A.M. Barakat, *Fuel* **280**, 1 (2020)
56. P.T.S. de la Cruz, K. Irikura, A. Lachgar, J.C. Cardoso, H.A. Cavero, M.V.B. Zanoni, *Electrocatalysis.* **11**, 546 (2021)
57. S. Bayani, H.R. Taghiyari, A.N. Papadopoulos, *Polymer (Basel)* **11**, 1 (2019)
58. K. Zhang, Y. Han, J. Qiu, X. Ding, Y. Deng, Y. Wu, G. Zhang, L. Yan, *J. Colloid Interface Sci.* **630**, 570 (2023)
59. Z. Jia, S.R. Rondiya, R.W. Cross, C. Wang, N.Y. Dzade, C. Zhang, *Electrochim. Acta.* **394**, 139143 (2021)
60. M.U. Anu Prathap, R. Srivastava, *Nano Energy.* **2**, 1046 (2013)
61. R.H. Tammam, A.M. Fekry, M.M. Saleh, *Int. J. Hydrogen Energy.* **40**, 275 (2015)
62. P.R. Jothi, S. Kannan, G. Velayutham, *J. Power Sources.* **277**, 350 (2015)
63. H. Sun, J. Liu, C. Zhang, Q. Yuan, Y. Ye, W. Yan, Z. Tian, C. Liang, *Carbon* **152**, 114 (2019)
64. Q. Luo, M. Peng, X. Sun, A.M. Asiri, *Catal. Sci. Technol.* **6**, 1157 (2016)
65. N. Spinner, W.E. Mustain, *Electrochim. Acta.* **56**, 5656 (2011)
66. M. Yu, S. Wang, J. Hu, Z. Chen, Y. Bai, L. Wu, J. Chen, X. Weng, *Electrochim. Acta.* **145**, 300 (2014)
67. R.S. Kate, S.A. Khalate, R.J. Deokate, *J. Alloys Compd.* **734**, 89 (2018)
68. L. Durai, S.S. Gunasekaran, S. Badhulika, *Int. J. Hydrogen Energy.* **47**, 3099 (2022)

Publisher's Note Springer Nature remains neutral with regard to jurisdictional claims in published maps and institutional affiliations.